# DEVELOPMENT OF NANOFABRICATED PROBES FOR SCANNING ELECTROCHEMICAL MICROSCOPY

By

**Nikoloz Nioradze**

B. S. in Chemistry, Tbilisi Technical University, Georgia, 1993

Submitted to the Graduate Faculty of

Arts and Sciences in partial fulfillment

of the requirements for the degree of

Master of Science

University of Pittsburgh

2010

UNIVERSITY OF PITTSBURGH

ARTS AND SCIENCES

This thesis was presented

by

Nikoloz Nioradze

It was defended on

November 24, 2009

and approved by

Shigeru Amemiya, PhD, Associate Professor

David Waldeck, PhD, Professor

Adrian Michael, PhD, Professor

Thesis Director: Shigeru Amemiya, PhD, Associate Professor

**DEVELOPMENT OF NANOFABRICATED PROBES FOR SCANNING ELECTROCHEMICAL MICROSCOPY**

Nikoloz Nioradze, M.S.

University of Pittsburgh, 2010

The work describes development of novel Pt disk electrodes with nanometer diameters using focused ion beam (FIB) milling. The nanofabricated electrodes are applied as probes of scanning electrochemical microscopy (SECM) for studying of electrochemical processes on redox reactive substrates. Nanotips are fabricated by pulling a platinum wire sealed in a glass capillary using a laser pipette puller. An inlaid platinum disk eventually is exposed by milling the tip of a pulled capillary by FIB. Electrodes are as small as 300-500 nm in diameter with a ratio of insulating glass sheath and Pt wire (RG) as small as 3. Moreover, FIB milling gives a flat tip surface. The small RG and smooth surface are helpful for approaching a probe close to a substrate in SECM feedback experiments. Nanometer-sized electrodes can be readily positioned within 100 nm from a polished platinum surface. After placing the tip close to the Pt disk, a potential of the Pt substrate is swept to drive a redox reaction, which is monitored as a current response at the nanometer-sized electrode. Presented method of combination of SECM and substrate cyclic voltammetry (CV) will allow for accurate extraction of electrochemical kinetic parameters of a redox reaction. Overall, it can be concluded that tips fabricated by presented method can be successfully exploited for SECM experiments. Described SECM-substrate CV approach will be useful for monitoring of electrochemical behavior of different conductive substrates.

## TABLE OF CONTENTS

## LIST OF TABLES

## LIST OF FIGURES

## LIST OF EQUATIONS

## PREFACE

The support of this work by National Institutes of Health (GM073439) and the Petersen Institute of NanoScience and Engineering (PINSE) at the University of Pittsburgh is gratefully acknowledged.

I thank Dr. Amemiya and his group and specially thank Jiyeon Kim for performing FIB milling and SEM measurements for nanofabricated electrodes.

# 1.0 INTRODUCTION

The main goal of this study is to develop nanometer-sized electrodes and apply them for investigation of electrochemical processes at various interfaces. To achieve this goal, the nanoelectrodes are employed as probes of scanning electrochemical microscopy[2] (SECM). As discussed in chapter 5, we envision SECM-based characterization of carbon nanomaterials as a future goal. Applications of our nanoelectrode probes, however, will not be limited to such solid electrode materials as discussed below.

## 1.1 APPLICATION OF NANOELECTRODES TO SECM

Traditionally, a micrometer-sized electrode has been employed as an SECM tip to scan in close proximity to a surface of interest. The electrochemical response of the tip (or of the substrate in response to the tip) provides quantitative information about the interfacial region. In the following, applications and advantages of SECM nanoprobes are described.

### 1.1.1 Rapid kinetic measurement

In general, the small size, reduced capacitance, increased temporal resolution and steady-state diffusion profiles all can be used to advantage in a number of application of nanoelectrodes.

As electrodes decrease in size, radial (3-dimensional) diffusion becomes dominant and results in faster mass transport that enables measurement of kinetics by steady-state experiments rather than by transient techniques. By decreasing electrode size from micrometer to nanometre scale at very high rates of mass transport, the electron transfer process is less likely to be limited by the diffusion of reactant to the electrode surface and study of faster electrochemical and chemical reactions should be possible [3, 4, 5, 6]

Mass transport rates at nanoelectrodes can be even higher when the electrodes are positioned near the conductive substrate by SECM Mirkin and co-workers demonstrated that very large standard rate constants of redox reactions at the tip (up to 17.0 cm/s) can be determined by steady-state voltammetry at the tip [6,7]

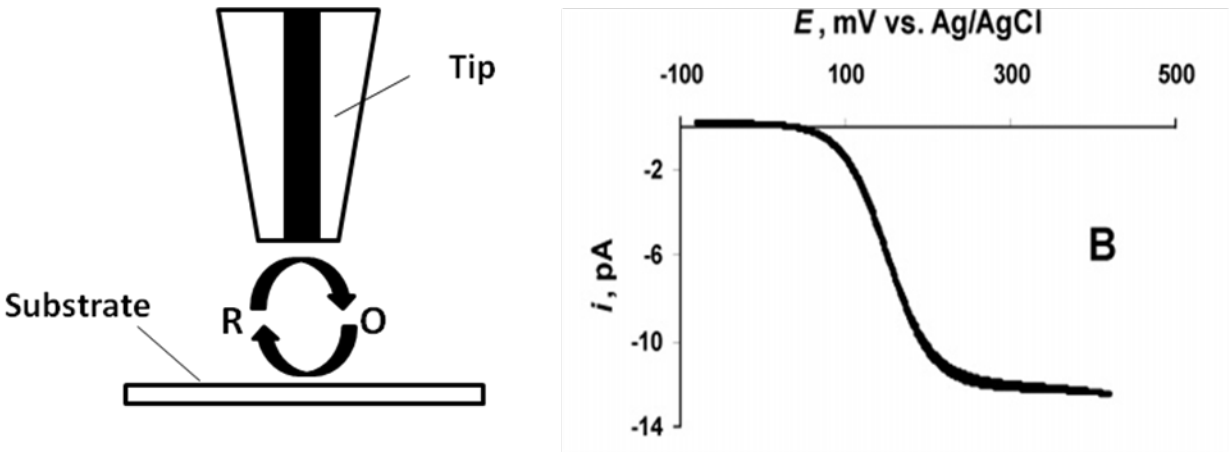


**Figure 1.** Steady state voltammetry obtained at nanotip placed at close vicinity over the conductive substrate

With their approach, the tip potential is swept linearly to electrolyze a redox mediator, R, to obtain a steady-state voltammetric tip response (right). The substrate potential is fixed such that a tip-generated species, O, is electrolyzed at the substrate to generate the original mediator at

a diffusion-limited rate. Subsequently, redox cycling in the nanometer-scale gap between the tip and substrate results in fast mass transfer.

Caution must be applied in such studies; when electrode dimensions approach molecular size and the diffusion layer becomes comparable to the electrical double layer then known diffusion principles cease to be relevant because of changes in solution properties (viscosity, density) [8,9] The influence of double layer on measured mass transport-limited currents at nanoelectrodes has been studied by a number of groups, especially those of White [10,11] and Kucernak [12,13]

### 1.1.2 SECM imaging.

SECM is useful for chemical imaging of various interfaces. The achievable spatial resolution of SECM imaging is effectively related to the size of the nanoelectrodes used for scanning. Applications of nanoelectrode probes in SECM are driven by the need to be able to map electrochemical activity of surfaces at greater resolution than is possible by micrometer sized electrodes. Several research groups developed nanotips for SECM imaging [14,15,16] For instance, Schumann and co-workers have used Pt nanodisc electrodes for the imaging of microfabricated structures. The needle-type Pt disk nanoelectrodes as extremely miniaturized scanning probes were tested for high resolution imaging of microstructure test samples produced by LIGA microfabrication technique. The imaging was performed in amperometric mode. Piezoelectric shear-force based distance control allowed not only a precise positioning Pt nanoelectrodes in close proximity to the surface of interest but also performing scanning and SECM imaging. So far, the best spatial resolution of the order of 1 nm was demonstrated by SECM imaging of

DNAs and enzymes immobilized on the wet mica surface, where the thin water layer serves as an electrolyte solution.[17]

### 1.1.3 Single molecule detection

A significant analytical challenge is electrochemical single molecule detection, which was realized by employing SECM. Achievement of this will enable various fundamental properties of isolated molecules to be studied. Bard and co-workers have observed behavior of a single molecule by trapping a small volume of a dilute solution of the electroactive species between an ultramicroelectrode tip with a diameter of ~15 nanometer and a conductive substrate.[18] They also exploited the ability of a recessed nanoelectrode to construct an extremely small volume thin-layer cell, when the protruding electrode surround is brought up to contact with a conducting surface.[19] As the tip is moved toward the surface one or more molecules were trapped within this volume. As they are oxidized at the nanoelectrode and reduced at the conducting substrate surface these electroactive molecules then diffuse back and forth between the electrode tip and the substrate enhancing the current response on the nanoelectrode.

Electrochemistry of individual molecules in zeptoliter volumes have been conducted to obtain information about mass transfer, adsorption, electron transfer kinetics, and double-layer effects on the nanoscale by using nanometer-sized cylindrical thin layer cell (TLC) formed by etching the surface of a disk-type platinum nanoelectrode 5- to 150-nm of radius[20]

## 1.2 NANOELECTRODE FABRICATION

To increase the spatial and time resolution of the SECM, it is imperative to develop methodologies for fabricating of tip electrodes having small dimensions and an appropriate shape allowing their close approach to a substrate. Nanoelectrods are fabricated usually by insulating an electrochemically etched metal wire with coatings with the exception of its apex. Various materials have been used to insulate metal wires, including glass, varnishes, wax, epoxy, paraffin, polymers, and electrophoretic paints.

Lewis and co-workers fabricated nanoelectrodes[3] based on sequential electrochemical etching of microwires to a fine tip and translating it through the molten glass bead. However the imperfect geometry of thus developed nanoelectrodes and their exploitation for study of reaction kinetics can lead to miscalculation of rate constants. [21] Bard and co-workers[5] used apiezon wax as the insulating material to prepare Pt electrodes; however they completely covered the tip so that it was insulated when tested under voltammetric conditions. An aperture in the wax was then opened by applying a 10 V bias between that insulated tip and a conducting substrate. This opened up a pore in the wax at the point of closest proximity to the substrate and the tip was then amenable to study by voltammetry and SECM.

Several groups introduced the use of electrophoretically-deposited paints to insulate the tip. Either cathodic or anodic deposition of paints can be employed.[22,14] Postpainting heat treatment is required in order to shrink the paint and force the tip of the etched metal cone to protrude.[23,10,24]

Mirkin and co-workers[25] prepared nanoelectrodes by pulling glass capillaries containing sealed microwires using a laser pipette puller; the pulling of the heated glass resulted in a

narrowing of both the glass and the wire within. Both the thickness of the eventual wire and its glass surround can be manipulated by controlling the conditions during the pulling procedure. After pulling of Pt wire - glass composite, platinum inlaid disk was exposed by mechanical polishing. Schuhmann and co-workers used the same strategy to fabricate needle-type disk shaped Pt- nanoelectrodes.[26] This approach appears to offer a more systematic methodology as well as polishable nanoelectrode surfaces, unlike the etching/insulation approach.

## 1.3 NAOSCALE VOLTAMETRY BY SECM

Fabrication of electrodes of ultra small dimensions and their exploitation with SECM technique opens the door to the use of steady-state voltammetry as a means of measuring kinetic parameters of fast electrochemical reactions.[27,28,29,30,31] These applications of nanoelectrodes in SECM kinetic studies, however, have been limited to reactions at the tip.

The purpose of this work is to develop an SECM method to voltammetrically investigate electrochemical reactions at the substrate. In our approach, the substrate potential is swept so that an original redox molecule or substrate-generated species is monitored at the tip, thereby yielding a unique voltammogram of tip current versus substrate potential (Figure 2). Specifically, when the tip is held at constant potential and is positioned at a fixed distance from the substrate, substrate potential, $E_s$, is swept linearly at a constant sweep rate to record a tip current response, *i*. If potential at tip is negative enough to reduce oxidized species at diffusion limited rate, potential is cycled on the substrate to obtain a cathodic wave of a voltammogram with increased $i_\infty$ (current at nanoprobe in the bulk solution) due to positive feedback (Figure 2, left). On the other hand, if potential at a tip is held positive enough to oxidize reduced species during

sweeping of substrate potential, anodic branch of voltammogram will be generated (Figure 2, right).

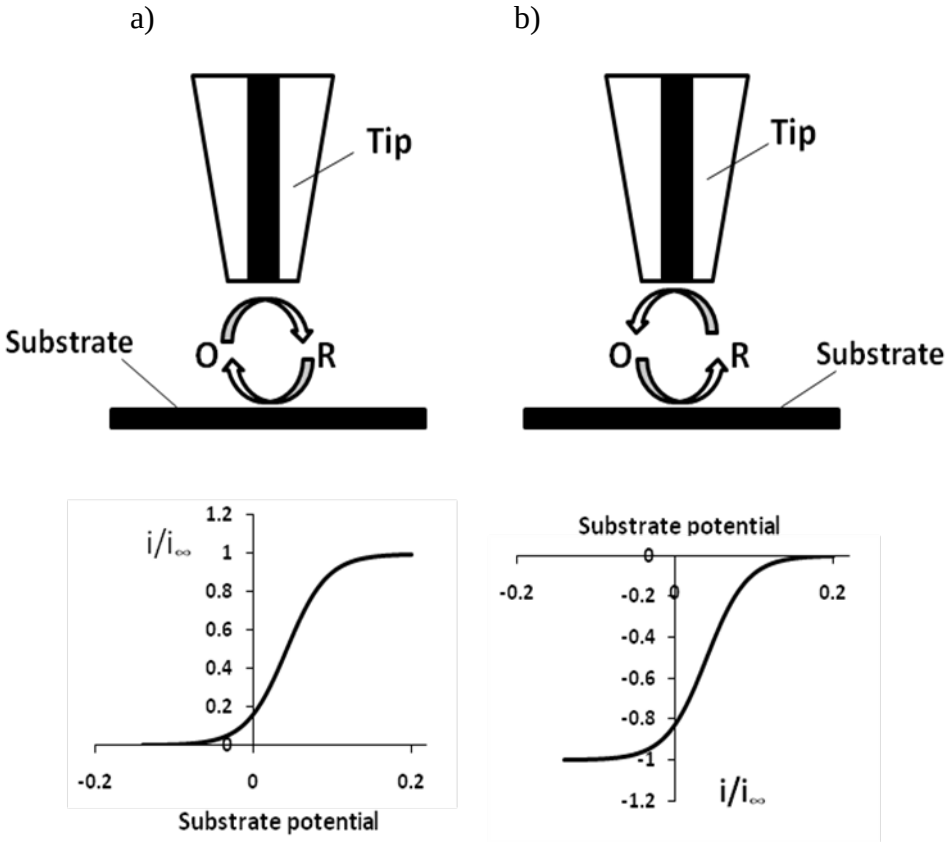


**Figure 2.** The principle scheme of nanoscale steady state voltammetry performed by using SECM a) Reduction wave generated when negative potential is held at the tip. b) Anodic wave, when positive potential is held at the tip. Current on y axis is normalized against current, $i_\infty$ at the tip in the bulk solution when only oxidized form of redox species is introduced in the system.

An important finding that I have made so far is that such a voltammogram is obtained under a steady-state condition when a nanometer-sized electrode is employed as a probe. Subsequently, no charging current, relative simplicity of data acquisition, and high accuracy and reproducibility of the results all are important advantages of our steady state measurements over the methods based on transient regime cyclic voltammetry (CV). Moreover, the proposed method allows for

monitoring electrochemical behavior of the substrate rather than tip[6] at nanoemeter scale and therefore local response from deferent regions of the substrate can be collected. Such nanoscale voltammetric measurements are also advantageous for the study of rapid charge transfer. Moreover, as a result having both cathodic as well as anodic polarization curves, unique combination of heterogeneous electron standard rate constant and transfer coefficient suitable for the whole voltammogram can be determined.[32,33]

## 1.4 SECM TIPS FOR NANOSCALE VOLTAMMETRY

To perform steady state voltammetry on a nanoscale level using SECM, several factors influencing the measurements should be considered. Kinetic regime can be observed on electrode if mass transfer rate, which is inversely proportional to electrode radius[31] is comparable to electron transfer process. More accurately, the gap size between nanotip and substrate rather than tip radius becomes a parameter affecting the mass transfer in SECM experiments when the tip approaches substrate at distance less than its radius. Therefore it is crucial to approach the tip very close to the substrate.

To be able to position the nanoprobe at a short distance, we fabricated Pt disk nanotips with thin insulating glass sheath using the method of simultaneous pulling of Pt micro wire and borosilicate glass capillary. The detailed procedure of tip fabrication is described in chapter Error! Reference source not found.. To expose the inlaid flat Pt disk after pulling and make smooth surface at nanoscale, we used the focused ion beam (FIB)[32] technique. This method uses a finely focused beam of ions (usually gallium) that can be operated at high beam currents for

site specific sputtering or milling. FIB allows to mill tip apex with the great control of a size and smoothness of the nanodisk.

# 2.0 NANOELECTRODE FABRICATION AND CHARACTERIZATION

Our approaches to fabrication of nanoelectrodes for SECM are described in this chapter. First, a Pt wire inserted into a borosilicate glass capillary is pulled by $CO_2$ laser-based puller to obtain a sharp Pt tip slightly exposed from a pulled capillary. The pulling condition was optimized to make a thin glass layer surrounding the Pt tip. Then, the electrode tip is polished mechanically or milled by FIB method to produce a disk-shaped Pt tip embedded in glass. The nanoelectrodes thus fabricated were characterized by optical microscopy, scanning electron microscopy, voltammetry, and SECM. We found that a polished tip is rough and even recessed, thereby limiting the possibility to position a tip close to substrate. On the other hand, FIB milling gives a smooth and flat tip, which is promising for SECM applications.

## 2.1 EXPERIMENTAL

### 2.1.1 Chemicals and materials

Hexaammineruthenium (III) chloride, 99%, was purchased from Strem Chemicals (Newburyport, MA,). Supporting electrolyte was 0.1M KCl (Fisher Science Education). Ferrocenemethanol (Aldrich, 97%) recrystallized twice from hexane. 0.2M NaCl (J.T. Baker,

assay 100%) was used as supporting electrolyte. All Aqueous solutions were prepared with deionized water (Nanopure water system, Barnstead) having resistivity more than 18.0 MΩ·Paragraph.

Borosilicate glass NA-51A custom glass tubing, with the length of 200mm, outer diameter 1mm and inner diameter 0.2mm leading to wall thickness 0.8mm was obtained from Drummond Scientific Company. Platinum wire (purity 99.99%, annealed, diameter 0.025mm) was obtained from Goodfellow. Copper-Nickel wire (diameter 0.13mm, hard) from Alfa Aesar. Ultra-Prep type A continues diamond lapping film (psa backing, diamond abrasive size 0.5 micron) was purchased from Buehler.

### 2.1.2 Equipment

Sutter instrument P-2000, $CO_2$ laser puller was used for microelectrode pulling. For visual characterization of electrodes optical microscope Olympus BX41 was used. Micro Forge (MF-900, Narishige, Japan) was used to assemble home build polishing instrument. Alignment of electrodes before polishing was monitored using a video microscope. CV and SECM measurements were performed by CHI 910B (CH Instruments Inc). All electrochemical measurements were conducted using faraday cage and vibration isolation table. Ag wire covered by AgCl was used as a reference electrode.

### 2.1.3 Nanoelectrode fabrication

Detailed procedures for nanoelectrode fabrication are described in the following.

Pulling: All materials were handled with gloves and kept free of dust and debris to eliminate sealing of contaminants into the glass along with the microwire. A 200 mm-long borosilicate glass capillary was cut to make two pieces of 95mm length. Capillaries were washed with acetone and dried in the oven under $140^0$C for ten minutes. A 25 μm-diameter Pt microwire was straightened and cut into a 20-25mm long piece. Twisting or introducing other mechanical stress may result in breaks in a pulled microelectrode. A 20 to 25 mm long Pt-wire was inserted into a 95 mm long borosilicate capillary with an outer diameter of 1 mm and an inner diameter of 0.2 mm in such a way that the Pt-wire was located in the middle part of the capillary. Ideally, two symmetric microelectrodes could be produced from a pull. Because of deferent melting temperatures of glass capillary (~ $700^0$C) and platinum ($1769^0$C), it is very important to choose right parameters in order to ensure simultaneous pulling of both glass capillary and Pt microwire. The pulling consisted of three steps; thinning of the composite (borosilicate glass capillary – Pt microwire), sealing of the Pt microwire with glass capillary, and puling. For the first, thinning step, the borosilicate capillary with Pt microwire inside was placed in the grooves of the laser puller bars and positioned inside the laser heating chamber so that the laser beam is focused on the center of the glass capillary. The laser beam is projected onto the back face of the glass by a reflective scanning mirror. Heat application to the glass is achieved by repeatedly scanning the mirror between the limits of a defined longitudinal area. The portion of the beam that is projected past the tubing is collected by a reflective concave mirror mounted behind the tubing. This retro-

reflective mirror or “retro mirror” redirects the divergent laser radiation onto the front side of the glass and thereby provides relatively uniform heating around the circumference of the glass.

A program that consists of two lines with the following parameter set was loaded:

HEAT=450, FIL=4, VEL=15, DEL: 120, PUL=0

HEAT=450, FIL=4, VEL=15, DEL: 120, PUL=0

where HEAT specifies the output power of the laser, FIL specifies the scanning pattern of the laser beam that is used to supply heat to the glass, VEL refers to velocity of the glass carriage system that is measured as the glass softens and begins to pull apart under a constant load and is determined by the viscosity of the glass as a measure of the glass temperature, DEL controls the time between when the HEAT turns off and when the hard pull is activated (the range of delay values (0-255) is time to allow the hard pull to be initiated at the same time as the deactivation of the laser when the delay value equals 128), and PUL controls the force of the hard pull.

The laser puller was activated four times and the particular shape of an assembly was obtained. The shape of the composite (Pt microwire and borosilicate glass capillary) after the first step is shown in Figure 3, a. After performing the first step, both ends of the capillary were connected to flexible silicone tubes and then to a vacuum pump via a Y-connector in order to remove air and to minimize bubble formation in the glass during the sealing. The safety shield of the P-2000 is not designed to support the vacuum tubes that are connected to the end of the capillary to be pulled. However it is possible to apply a vacuum to a capillary without interfering with the safety mechanisms of the pipette puller. To ensure that the instrument exerts no pulling force on the capillary during the sealing step, home made stoppers were placed on each of the pulling sleds. When the capillary was sufficiently evacuated (Millitorr vacuum gauge reading), a heating program was applied to seal several millimeters of the microwire into the borosilicate

capillary. In the second step a tight contact between the glass walls of the capillary and the inserted Pt-wire has to be assured. It is crucial to make particular ratio of sealed Pt microwire and glass wall in order to minimize the ratio of glass sheath and Pt microwire after pulling. Parameters for the sealing were as follows:

The laser puller was activated four times and the particular shape of an assembly was obtained. The shape of the composite (Pt microwire and borosilicate glass capillary) after the first step is shown in Figure 3, a. After performing the first step, both ends of the capillary were connected to flexible silicone tubes and then to a vacuum pump via a Y-connector in order to remove air and to minimize bubble formation in the glass during the sealing. The safety shield of the P-2000 is not designed to support the vacuum tubes that are connected to the end of the capillary to be pulled. However it is possible to apply a vacuum to a capillary without interfering with the safety mechanisms of the pipette puller. To ensure that the instrument exerts no pulling force on the capillary during the sealing step, home made stoppers were placed on each of the pulling sleds. When the capillary was sufficiently evacuated (Millitorr vacuum gauge reading), a heating program was applied to seal several millimeters of the microwire into the borosilicate capillary. In the second step a tight contact between the glass walls of the capillary and the inserted Pt-wire has to be assured. It is crucial to make particular ratio of sealed Pt microwire and glass wall in order to minimize the ratio of glass sheath and Pt microwire after pulling. Parameters for the sealing were as follows:

Heat=450, Fil=4, V=12, D=120, Pul=0

In a first heating sequence, the evacuated glass capillary has been heated for 4 seconds. After this time, the heating was stopped and the composite was cooled down for 3 seconds. The second turn of the heating was applied for 10 seconds so that thickness of the glass was made down to

0.07-0.075mm. As a result the assembly with the particular ratio of sealed intact Pt microwire and borosilicate glass was obtained (Figure 3, b). After the second step, stoppers were removed and a glass capillary was detached from the vacuum pump.

The last step was pulling step, which results in making of a pair of pulled tips (Figure 3, c). Due to the fast and reproducible local heating of a glass capillary together with an inserted metal wire, the metal wire was pulled simultaneously with the glass, thereby leading to a drastic decrease of its diameter and a simultaneous tight seal of the metal within the glass capillary.Following pulling parameters consisting of only one line was loaded on the composite

HEAT=350 FIL=3 VEL=15 DEL=120 PUL=120

Based on desirable size of the tip apex, PUL parameter can be changed down to zero so that an electrode of a bigger size can be produced without significant changing of the ratio of Pt wire and glass thickness.

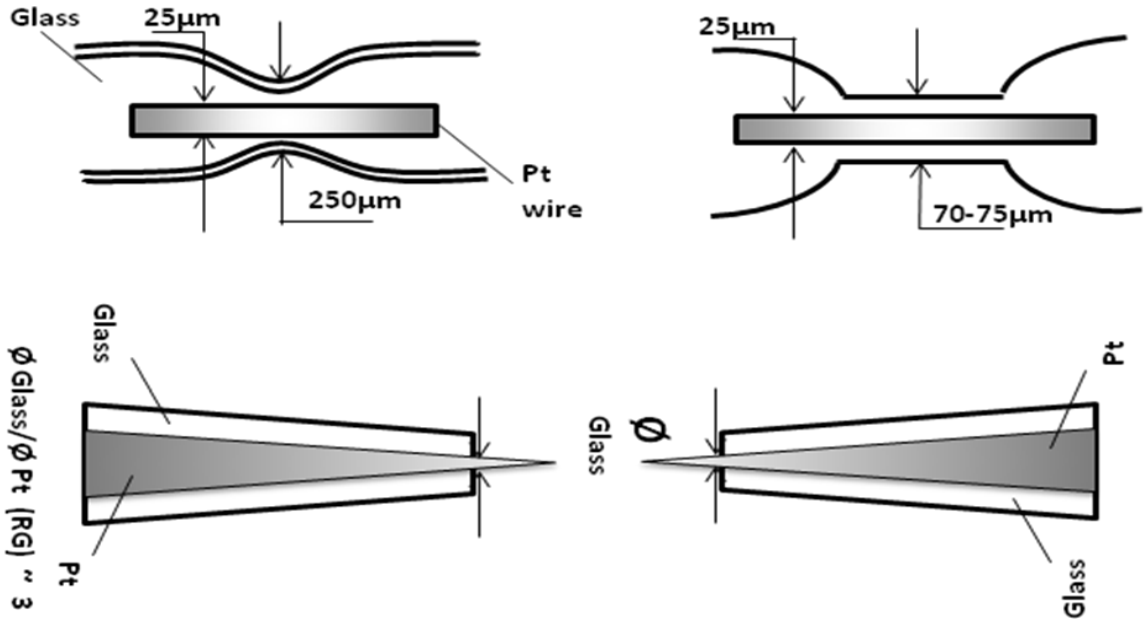


**Figure 3.** Steps of pulling process: a) thinning, b) sealing c) a pair of microelectrodes after pulling ; Øglass/ØPt~3-4

A success rate of fabrication of microtips by this method can be as high as 70-80%. The outcome can vary time to time and in that case parameters (especially for the second and third steps) should be adjusted.

After fabrication of a pair of electrodes, an electrical contact was made between the pulled Pt wire and a copper-nickel wire. A 0.13mm hard copper-nickel wire was inserted into the capillary without using any paste and the rest of the Pt microwire was jammed due to pushing down the copper-nickel wire. After making a contact between Pt microwire and the copper-nickel wire, the end of the glass capillary was sealed with epoxy (Devcon).

As a result of pulling, conical shape of Pt wire followed tapered part of the glass capillary. The ratio of glass sheath and metal was usually 3-5 based on the segment of the tapered part. Conical shape of the pulled Pt electrode made it possible to fabricate any size Pt inlaid disk electrode with relatively small ratio of Pt disk diameter and glass sheath thickness either by mechanical polishing or FIB milling.

Polishing: For the polishing of insulated microelectrodes, a home built setup was used. A 15VDC motor with a gear was mounted on the micro forge stage equipped with a microscope (MF-900, Narishige). A diamond lapping film with abrasive size 0.5 micron was immobilized on the gear of the motor. Alignment of the tip against diamond film was monitored by video microscope and the microscope of the micro forge instrument. Electrodes were positioned over the diamond lapping film while the mechanical polishing process was monitored with the microscope on the micro forge stage.

The most critical component of this step is the ability to stop polishing precisely at the moment when a disk of desired radius is created. Due to the conical shape of the pulled metal tips, slight overpolishing results in electrodes with radii larger than desired.

Milling of Electrodes by Focused Ion Beam Technique (FIB): Due to difficulty of controlling of electrode diameter and surface smoothness by mechanical polishing, focused ion beam technique was exploited to conduct the final step of microelectrode fabrication. FIB allows for more precisely controlling dimensions of an exposed platinum disk and glass sheath than mechanical polishing.

### 2.1.4 Nanoelectrode characterization

Characterization by Optical Microscopy and Scanning Electron Microscopy (SEM) After pulling process, electrodes were observed by optical microscope (Olympus BX41) to check the size and ratio of Pt wire against insulating glass. The shape and size of electrodes at micrometer scale were checked by optical microscopy to obtain the side view of polished tips as well as their top view shows SEM images of as pulled, polished, and FIB-milled tips. The pictures clearly indicate contrast between mechanically polished and FIB milled tips in terms of smoothness of either glass or platinum surfaces.

a) b)

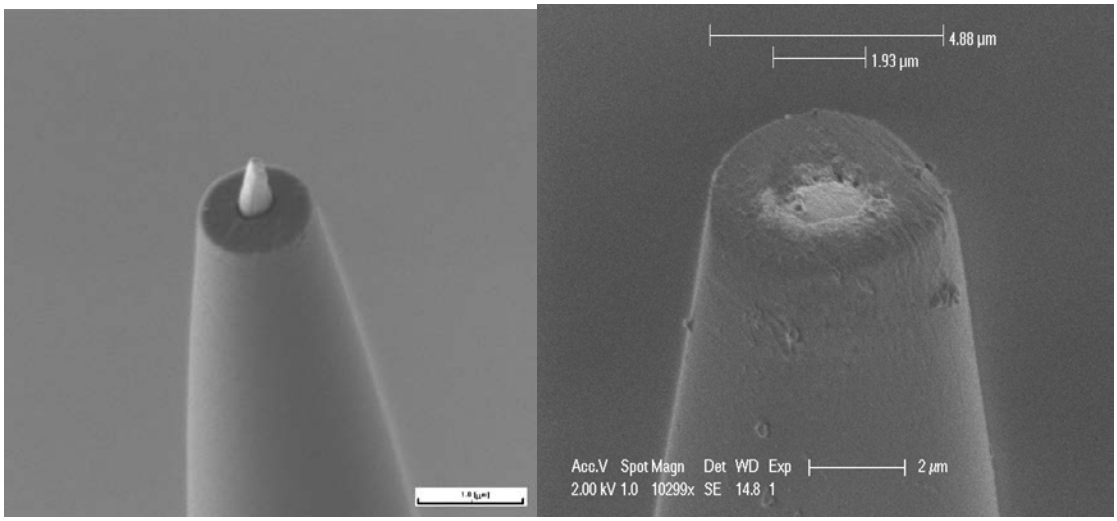


c)

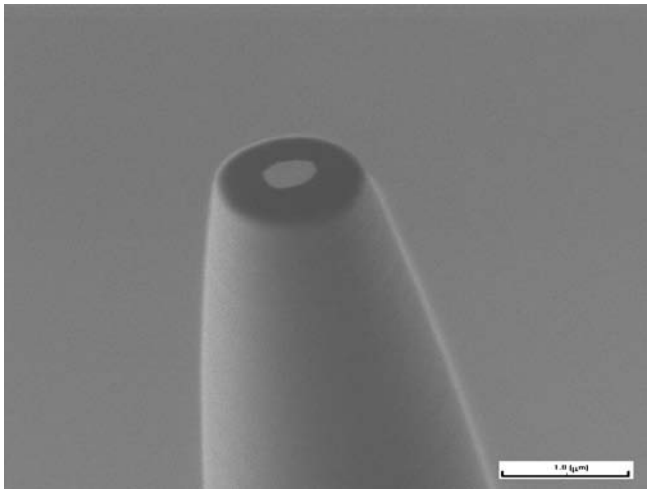

**Figure 4.** SEM images of pulled microelectrode: a) before polishing, b) after polishing, c) FIB milled electrode

Electrochemical Characterization: CV and SECM The voltammetric behavior of fabricated electrodes was evaluated using hexammineruthenium (III) chloride (1mM $Ru(NH_3)_6Cl_3$ in 1M KCl) or feroccenemethanol (0.5mM FcMeOH in 0.2M NaCl) redox systems. The apparent radius

of a disk can be determined by measuring the steady state diffusion-limited current, $i_d$, in a solution containing a known concentration of a redox-active molecule (eq. 1).

$$i = 4xnFDc^* a \qquad 1$$

D and c* are the diffusion coefficient and bulk concentration of the electroactive species respectively, n is the number of electrons transferred per molecule, F is Faraday constant, a is the tip radius, and the geometric factor, $x$ is a function of RG (=$r_g/a$; $r_g$ is the outer wall radius), which was tabulated[35] and expressed by an analytical approximation.[36] Other electrode geometries, however, also give a limiting current given by a similar equation so that eq. **1** is useful only in providing a rough estimate of the exposed surface area of the electrodes. To evaluate accurately the shape and size of polished and FIB-milled electrodes, SECM approach curves were measured. Figure 5 shows cyclic voltammogram and SECM approach curve of polished microelectrode with radius of 0.69 µm and RG 3.0 made on insulator glass substrate.

a) b)

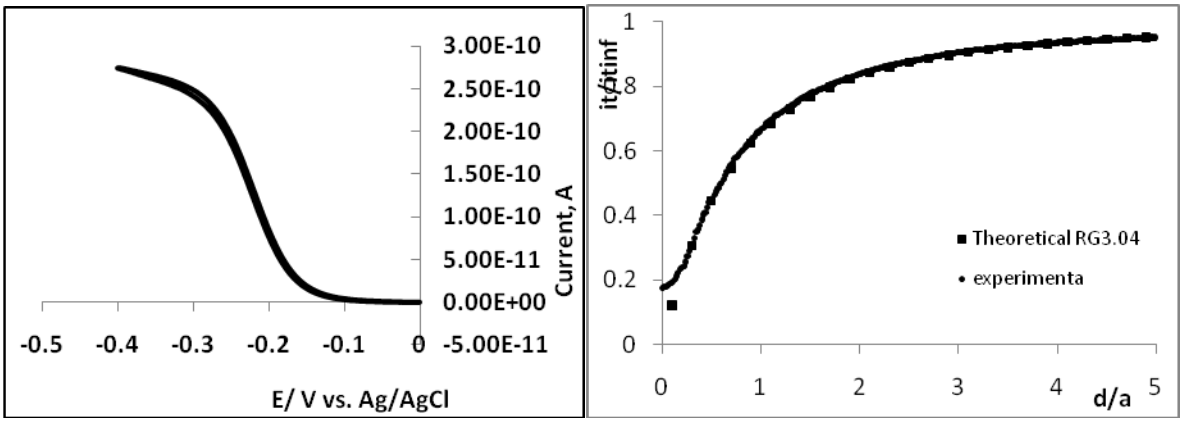


**Figure 5.** (a) Cyclic voltammetry and (b) SECM approach curves for polished electrodes

For polished electrodes, an experimental approach curves fits with a theoretical one only down to the normalized distance of 0.3–1 even when the electrode radius is relatively large (~0.7 μm). These closest distances are not good enough for SECM applications. Moreover, the size and shape of the rough, recessed tip are not accurately evaluated by theoretical analysis of the approach curves because an inlaid disk shape is assumed in theoretical model.

Figure 6 shows cyclic voltammetry and SECM approach curves for a 225 nm-radius FIB milled tip. The Approach curve was made in FcMeOH solution on glass insulator substrate.

a) b)

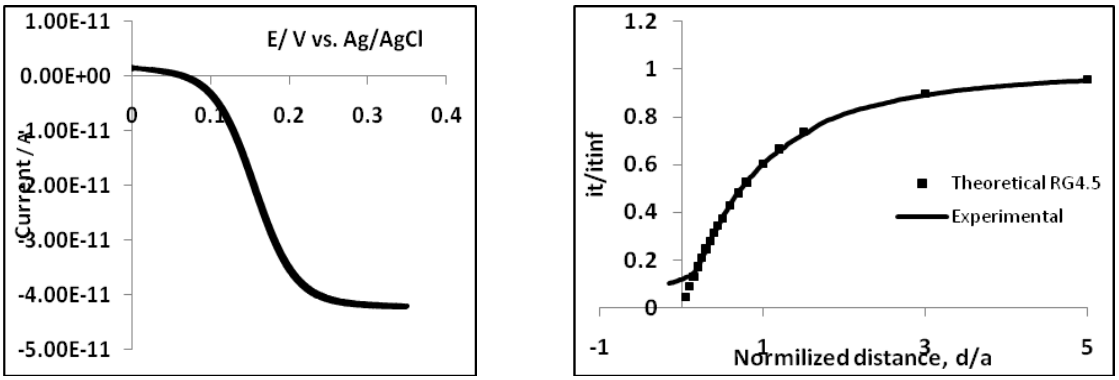


**Figure 6.** Cyclic voltammetry (a) and SECM approach curves (b) for FIB milled microelectrode. Electrode radius is 225nm, approach distance 34nm

0.15-0.2 is typical achievable normalized distance for FIB milled tips with a radius as small as 225 nm. As SEM image as approach curves show advantage FIB milled tips against polished ones.

Even though simultaneous pulling is relatively easy and quick method to make submicrometer size electrodes, there is a problem that should be addressed. We observed that electrodes after some period of time (usually 2–3 days) undergo shrinking process and exposed platinum tip is buried in glass insulator. Figure 7 shows SEM images of a tip before and after shrinking process.

a) b)

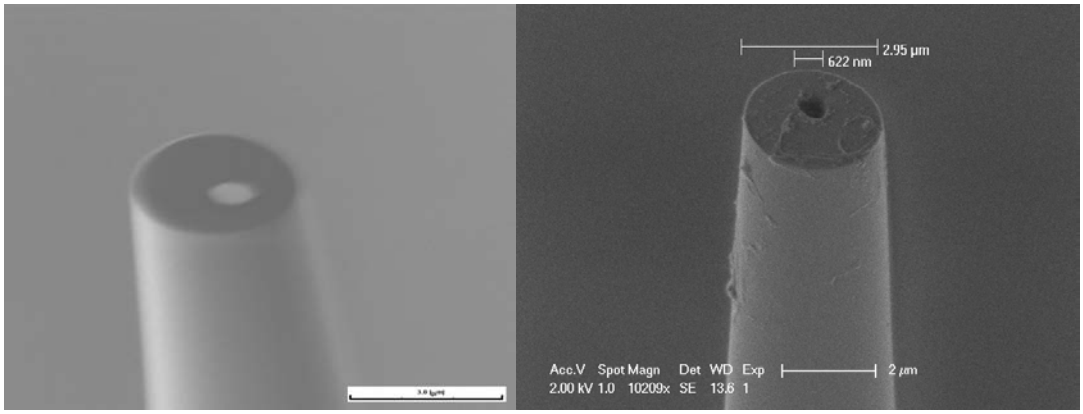


**Figure 7.** SEM images of tips a) before and b) after shrinking

One explanation for this tip shrinkage might be that, after pulling, stretched Pt wire tends to be relaxed and it does not have sufficiently tight contact with insulating glass to prevent shrinking process. We systematically monitored tips by optical microscope and by the value of diffusion limited current and also periodically by SEM. Only tips that showed stable geometry were used to collect experimental data.

## 2.2 CONCLUSIONS

Simultaneous pulling of Pt microwire and borosilicate glass capillary with particular pulling parameters described above is a convenient method to fabricate in short period of time microelectrodes of different sizes with relatively small RG from 3 to 5. Such electrodes after FIB milling can be positioned close to a substrate surface. On the other hand, SEM images and approach curves of mechanically polished microelectrodes at this point show unsatisfactory results. Better polishing procedure proposed by Mirkin and co-workers is required for obtaining

high quality nanotips [6,25] Along with advantages there is a problem of tip shrinking. Currently we study the reason of recession in order to further improve tip fabrication.

# 3.0 NANOSCALE STEADY STATE VOLTAMMETRY

FIB-milled nanoelectrodes were employed to carry out proof-of-concept experiments for nanoscale voltammetry, which was proposed in chapter Error! Reference source not found. (see Figure 2).

## 3.1 EXPERIMENTAL

### 3.1.1 Chemicals and instrumentation

Ferrocenemethanol (Aldrich, 97%, St. Louis, MO) was recrystallized twice from hexane, 0.2M NaCl (J.T. Baker, assay 100%) was used as supporting electrolyte. All Aqueous solutions were prepared with deionized water (Nanopure water system, Barnstead) having resistivity more than 18.0MΩ·cm.

CV and SECM were performed by CHI 910b, CH instrument Inc. All electrochemical measurements were conducted using faraday cage and vibration isolation table.

### 3.1.2 Results and discussion

To test the concept of nanoscale steady state voltammetry for a reversible case, FcMeOH was employed as a redox mediator. Figure 8 shows a steady-state voltammogram at a 288 nm-radius nanometer size tip in bulk of 0.5 mM FcMeOH solution with 0.2 M NaCl supporting electrolyte. The tip size was comparable to the size determined from an SEM image (Figure 9).

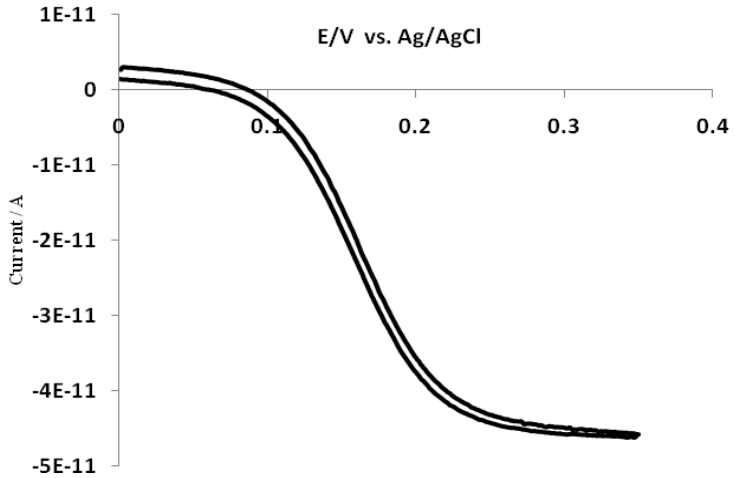


**Figure 8.** A steady state voltammogram of 0.5mM ferrocenemethanol and 0.2M NaCl

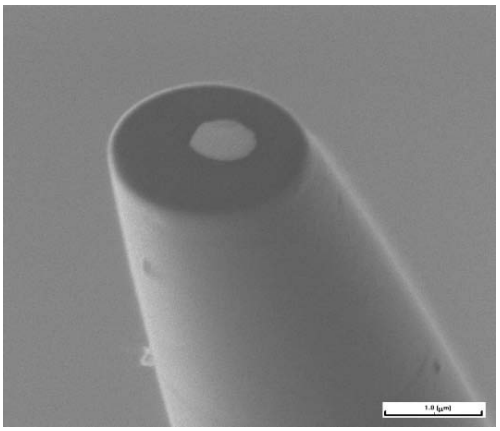

**Figure 9.** SEM image of nanotip showing inlaid Pt disk with diameter 0.575-0.621 µm and glass sheath with diameter 1.995µm giving RG close 3.3

This electrode was approached to a Pt substrate to obtain steady-state voltammograms of FcMeOH under an SECM configuration. The tip was loaded with a constant potential that is positive enough to oxidize FcMeOH at diffusion limited reaction rate. Figure 10 represents approach curves on a biased, mirror-polished Pt substrate, where the tip touches the Pt substrate (Figure 10, a) or stopped at 0.4 normalized distance from the substarte (Figure 10, b). For the first case, the tip current increased significantly due to direct electrical contact of the nanoelectrode with a Pt disk substrate. This phenomena confirms that the Pt nanotip is not recessed and that the glass sheath around the tip is thin enough not to hinder the Pt tip approaching to the substrate.

a) b)

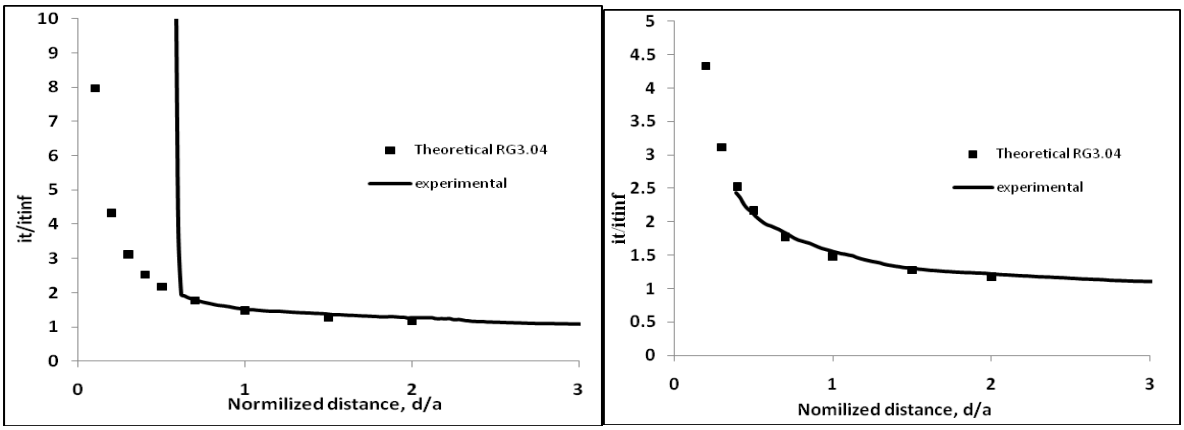


**Figure 10.** Approach curves on Pt substrate a) electrode touched the Pt disk b) the tip stopped over substrate at 0.4 normalized distance. (lines experimental, squares theoretical curves)

After positioning the tip at 0.4 normalized distance i.e., 80 nm, from the Pt substrate, the potential at the Pt substrate was swept and tip current was monitored. While a voltammogram on the big Pt substrate had a well-defined peak shape, steady-state currents were obtained at the Pt nanotip as demonstrated by a sigmoidal, traceable shape of the plots of the tip current vs substrate potential (Figure 11). When the tip potential was positive enough during the potential

sweep, an anodic branch of a steady-state voltammogram was obtained. On the other hand, a sufficiently negative tip potential resulted in a cathodic branch of a steady-state voltammogram.

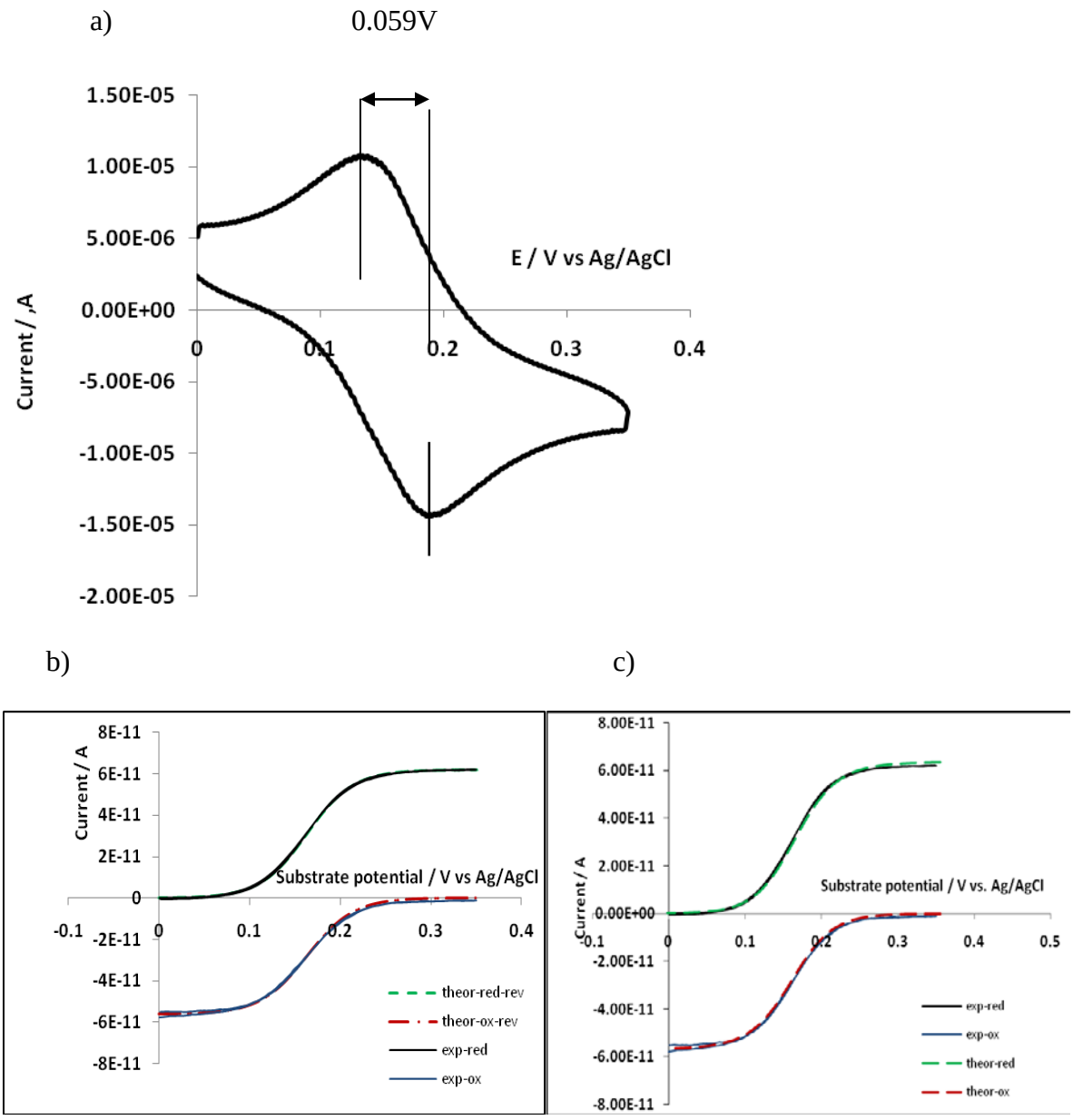


**Figure 11.** a) Reversible peak shaped cyclic voltammogram on Pt substrate b) Fit of steady state voltammograms on Pt nanotip and curves calculated by eq. 2 c) Fit of steady state voltammograms on Pt nanotip and curves obtained by finite element simulation

The cyclic voltammogram (Figure 11, a) at the big substrate is reversible and gives a peak separation of 59mV. Steady-state voltammograms (Figure 11, b,c) at nanotip overlay perfectly with theoretical curves calculated by equation describing voltammogram for a reversible system (dashed green for the cathodic, dashed red for the anodic)

$$E = E_{1/2} + \frac{RT}{zF} \ln\left(\frac{i_d - i}{i}\right) \qquad 2$$

where $E_{1/2}$ is the half-wave potential, $i_d$ is diffusion limited current, and i current at any point of voltammetric curve. The steady-state voltammograms also fit well with reversible curves

(Figure 11, c) dashed green for the cathodic and dashed red for the anodic) obtained by finite element simulation (see Appendix 1) with a dimensionless kinetic parameter of K > 10 (equation **3**)

$$K = \frac{k^0 * a}{D} \qquad 3$$

where $k^0$ is standard rate constant, *a* is a tip radius and D diffusion coefficient. With a = 204nm and D = 7.8E-6 $cm^2/s$ in eq 3, $k^0$ was estimated to be 3.3cm/s or greater, which is consistent with a reported value of 6.8cm/s.[6]

## 4.0 KINETIC EFFECT ON NANOSCALE VOLTAMMOGRAMS

Charge-transfer reactions at the nanoscale region of the substrate surface under an SECM nanotip can be kinetically limited, thereby allowing for determination of their kinetic parameters. Absence of the limitations caused by the charging current, relative simplicity of data acquisition, and high accuracy and reproducibility of the results all are important advantages of steady-state measurements by this nanoscale voltammetric method. On the other hand, a transient CV (see Figure 11a) is more informative than a steady-state voltammogram.[37] A single transient CV with both anodic and cathodic branches gives all parameters in the Butler-Volmer-type model when it is obtained under kinetic limitations. In contrast, if only one type of redox species is introduced in the system, steady-state voltammetry gives only a positive or a negative current response. Therefore, analysis based only on one branch of voltammogram not knowing the shape of the other one can lead to errors during estimation of unique combination of kinetic parameters such as standard rate constant, $k^0$ and transfer coefficient, $\alpha$. In fact, there might be several different combinations of $k^0$ and $\alpha$ which would satisfy the same curve of voltammogram. This limitation of steady-state voltammetry is illustrated by simulated nanoscale voltammograms in Figure 12, where a standard rate constant was assumed to be equal to a mass transfer coefficient. These voltammograms depend on transfer coefficients very weakly especially for $\alpha \geq 0.5$ in an anodic branch and $0.5 \geq \alpha$ in a cathodic branch. Subsequently, $\alpha$ value can not be determined from such a steady-state voltammogram of fast charge transfer. Moreover, a $k^0$ value may be overestimated

(or underestimated) by employing an inaccurate α value in data analysis. This limitation, however, can be overcome when both cathodic and anodic steady state voltammograms are available. For instance, an anodic voltammogram with α = 0.5 is very different from that with α = 0.3 while the corresponding cathodic voltammograms are very similar. I plan to demonstrate this advantage of nanoscale voltammetry experimentally using a slower redox couple than ferrocenemethanol.

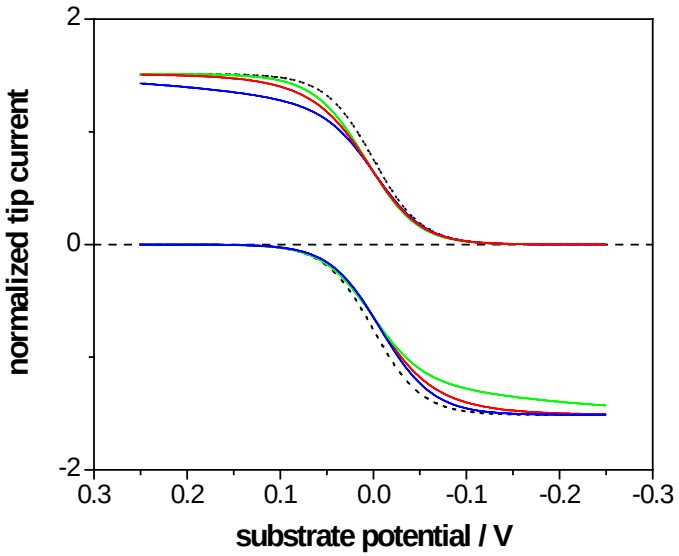


**Figure 12.** Plots of tip current versus substrate potential for a reversible reaction (black dotted line) and quasi- reversible reactions with $K$ (= $k^0a/D_O$) = (a) 1 and $\alpha$ = 0.2 (green line), 0.5 (red line), and 0.8 (blue line).

## 5.0 FUTURE PLANS

The main target of our future research will be the study of electrochemical reactivity of carbon nanomaterials such as highly ordered pyrolitic graphite (HOPG) [38,39,40] and single-walled carbon nanotubes (CNT) [41,42] using the proposed method of nanoscale steady state voltammetry (Figure 13).

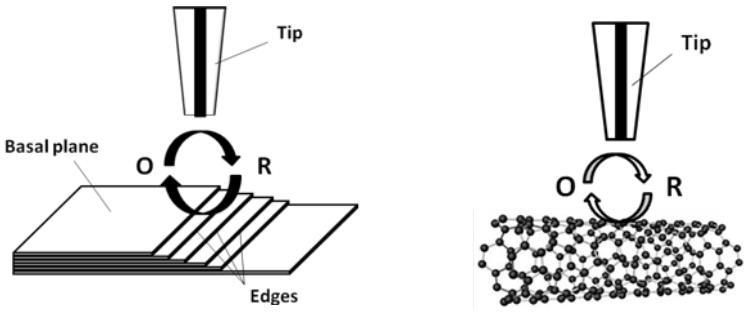


**Figure 13.** Nanoscale steady-state voltammetry a) at highly ordered pyrolitic graphite (HOPG) and b) single walled carbon nanotube

There has been much excitement about the prospect of CNTs as new carbon electrode materials, particularly for electroanalysis. Questions, however, remain regarding the fundamental electrochemical properties of CNTs to be solved. CNT based electrodes show very high electrochemical reactivity, which is not observed on conventional carbon electrodes.[43] We plan to explore CNT surface electrochemical reactivity applying nanoscale steady-state voltammetry. Our group demonstrated the first application of SECM to the study of individual SWNTs to find

that their redox reactivity apparently varies with their chirality.[44] This finding is supported by theory of SWNT electrochemistry.[45] Moreover, our SECM study demonstrated that the sidewall of the SWNT is highly active for electron transfer. However, a detailed kinetic study of various SWNTs by SECM voltammetry developed in my work is required for understanding of the structure-reactivity relationship.

I also plan to study HOPG for a comparison with SWNTs. Electrochemical behavior of HOPG is greatly controlled by its surface condition. Traditionally, their edges have been considered to be responsible for reactivity of the surface. On one hand, its $sp^2$-basal plan mimics the sidewall of SWNTs although their electronic structures are significantly different. On the other hand, edge planes are separated by the basal panes while traditional voltammetry [46,47] does not resolve reactivity of each edge plane from that of basal plane; nanoscale steady state voltammetry should be applied to spatially resolve redox reactivity of this heterogeneous surface.

# APPENDIX A

## COMSOL MULTIPHYSICS SIMULATION

An SECM diffusion problem with a pair of disk-shaped UMEs as a probe and a substrate is defined in a cylindrical coordinate (Figure 14). In comparison to the tip, the substrate is infinitely large, thereby limiting the simulation space in *r* direction. The simulation space limit in z direction is large enough for development of a planar diffusion layer from the substrate. Initially, the solution phase contains only one redox-active mediator, O, which is reduced to R at the tip (O + e $\rightarrow$ R). Diffusion of O and R in the solution phase can be expressed as

$$\frac{\partial c_{\mathrm{O}}(r,z)}{\partial t} = D_{\mathrm{O}}\left[\frac{\partial^2 c_{\mathrm{O}}(r,z)}{\partial r^2} + \frac{1}{r}\frac{\partial c_{\mathrm{O}}(r,z)}{\partial r} + \frac{\partial^2 c_{\mathrm{O}}(r,z)}{\partial z^2}\right] \qquad \text{A1}$$

$$\frac{\partial c_{\mathrm{R}}(r,z)}{\partial t} = D_{\mathrm{R}}\left[\frac{\partial^2 c_{\mathrm{R}}(r,z)}{\partial r^2} + \frac{1}{r}\frac{\partial c_{\mathrm{R}}(r,z)}{\partial r} + \frac{\partial^2 c_{\mathrm{R}}(r,z)}{\partial z^2}\right] \qquad \text{A2}$$

where $c_{\mathrm{O}}(r,z)$ and $c_{\mathrm{R}}(r,z)$ are local concentrations of the respective mediators with diffusion coefficients of $D_{\mathrm{O}}$ and $D_{\mathrm{R}}$. The tip reaction is assumed to be diffusion-limited, thereby yielding a boundary condition at the tip as

$$c_{\mathrm{O}}(r,z) = 0 \qquad \text{A3}$$

$$c_{\mathrm{R}}(r,z) = c_0 \qquad \text{A4}$$

On the other hand, a quasi-reversible substrate reaction gives the corresponding boundary condition as

$$D_{\mathrm{O}}\left[\frac{\partial c_{\mathrm{O}}(r,z)}{\partial z}\right]_{z=d} = k_{\mathrm{b,s}}c_{\mathrm{R}}(r,d) - k_{\mathrm{f,s}}c_{\mathrm{O}}(r,d) \qquad \text{A5}$$

$$D_{\mathrm{R}}\left[\frac{\partial c_{\mathrm{R}}(r,z)}{\partial z}\right]_{z=d} = k_{\mathrm{f,s}}c_{\mathrm{O}}(r,d) - k_{\mathrm{b,s}}c_{\mathrm{R}}(r,d) \qquad \text{A6}$$

with

$$k_{\mathrm{f,s}} = k^0 \exp\left[-\frac{\alpha F(E - E^{0'})}{\mathrm{RT}}\right] \qquad \text{A7}$$

$$k_{\mathrm{b,s}} = k^0 \exp\left[\frac{(1-\alpha)F(E - E^{0'})}{\mathrm{RT}}\right] \qquad \text{A8}$$

The other boundary conditions are given in Figure 14.

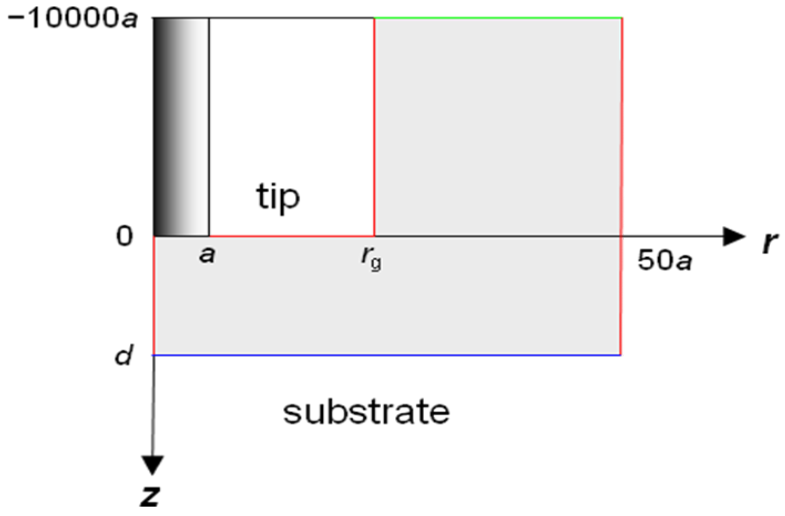


**Figure 14.** Geometry of the SECM diffusion problem in the cylindrical coordinate

There is no normal flux at the red boundaries while the green boundary represents simulation space limits. The boundary conditions at the tip and substrate (black and blue,

respective An SECM diffusion problem was solved in a dimensionless form using COMSOL Multiphysics. Dimensionless parameters are defined by:

$$R = r/a \quad \text{A9}$$

$$Z = z/a \quad \text{A10}$$

$$\mathrm{RG} = r_g/a \quad \text{A11}$$

$$L = d/a \quad \text{A12}$$

$$C_O(R,Z) = c_O(r, z)/c_0 \quad \text{A13}$$

$$C_R(R,Z) = c_R(r, z)/c_0 \quad \text{A14}$$

$$\gamma = D_R / D_O \quad \text{A15}$$

$$\tau = 4Dt/a^2 \quad \text{A16}$$

$$\sigma = \frac{a^2}{4D_O}\frac{nFv}{RT} \quad \text{A17}$$

$$\kappa = \frac{k^0 a}{D_0} \quad \text{A18}$$

Diffusion of O and R in the solution phase can be expressed in the dimensionless form as

$$\frac{\partial C_{\mathrm{O}}(R,Z)}{\partial \tau} = 0.25\left[\frac{\partial^2 C_{\mathrm{O}}(R,Z)}{\partial R^2} + \frac{1}{R}\frac{\partial C_{\mathrm{O}}(R,Z)}{\partial R} + \frac{\partial^2 C_{\mathrm{O}}(R,Z)}{\partial Z^2}\right] \qquad \text{A19}$$

$$\frac{\partial C_{\mathrm{R}}(R,Z)}{\partial \tau} = 0.25\gamma\left[\frac{\partial^2 C_{\mathrm{R}}(R,Z)}{\partial R^2} + \frac{1}{R}\frac{\partial C_{\mathrm{R}}(R,Z)}{\partial R} + \frac{\partial^2 C_{\mathrm{R}}(R,Z)}{\partial Z^2}\right] \qquad \text{A20}$$

The values of 0.25 and $0.25\gamma$ in eqs 22 and 23, respectively, were used as dimensionless diffusion coefficients in the simulation. The substrate boundary conditions are now given by

$$0.25\left[\frac{\partial C_{\mathrm{O}}(R,Z)}{\partial Z}\right]_{Z=L} = \frac{0.25\lambda}{\theta_{\mathrm{S}}^{\alpha}}[\theta_{\mathrm{S}} C_{\mathrm{R}}(R,Z) - C_{\mathrm{O}}(R,Z)] \qquad \text{A21}$$

$$\frac{0.25}{\xi^2}\left[\frac{\partial C_{\mathrm{R}}(R,Z)}{\partial Z}\right]_{Z=L} = \frac{0.25\lambda}{\theta_{\mathrm{S}}^{\alpha-1}}\left[\frac{C_{\mathrm{O}}(R,Z)}{\theta_{\mathrm{S}}} - C_{\mathrm{R}}(R,Z)\right] \qquad \text{A22}$$

With

$$\theta_{\mathrm{S}} = \exp\left[\frac{F}{RT}(E - E^{0'})\right] \qquad \text{A23}$$

Eqs 24 and 25 are equivalent to the expression of the flux boundary condition in COMSOL Multiphysics. The other boundary conditions and the initial condition are also given in the dimensionless form. The resulting tip current is obtained in the dimensionless form with respect to the limiting current at a disk probe with infinite RG, yielding

$$I_{\mathrm{T}} = \frac{i_{\mathrm{T}}}{i_{\mathrm{T},\infty}} = \frac{\pi}{2}\int_0^{b/a} R\left[\frac{\partial C(R,L)}{\partial Z}\right] dR \qquad \text{A24}$$

Where

$$i_{\mathrm{T},\infty} = 4nFD_{\mathrm{O}}c_0 \qquad \text{A25}$$

An example of the simulation result for a quasi-reversible substrate reaction is attached.

## APPENDIX B

## COMSOL MODEL REPORT

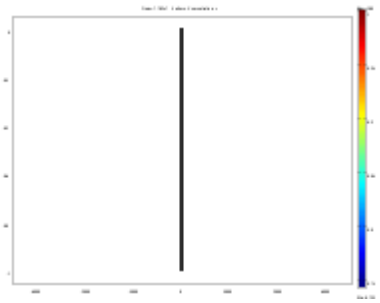

**Figure 15.** Comsol model

- Title - COMSOL Model Report
- Table of Contents
- Model Properties
- Geometry
- Geom1
- Integration Coupling Variables
- Solver Settings
- Postprocessing
- Variables

**Table 1.** Comsol model report

| Property | Value |
|---|---|
| Model name | |
| Author | |
| Company | |
| Department | |
| Reference | |
| URL | |
| Saved date | Jul 14, 2009 3:41:27 PM |
| Creation date | Mar 17, 2007 1:13:01 PM |
| COMSOL version | COMSOL 3.5.0.608 |

File name: C:\CV-SECM.mph

Application modes and modules used in this model:

- Geom1 (Axial symmetry (2D))
  - Diffusion (Chemical Engineering Module)
  - Diffusion (Chemical Engineering Module)

**3.0 Geometry**

Number of geometries: 1

### 3.1 Geom.1

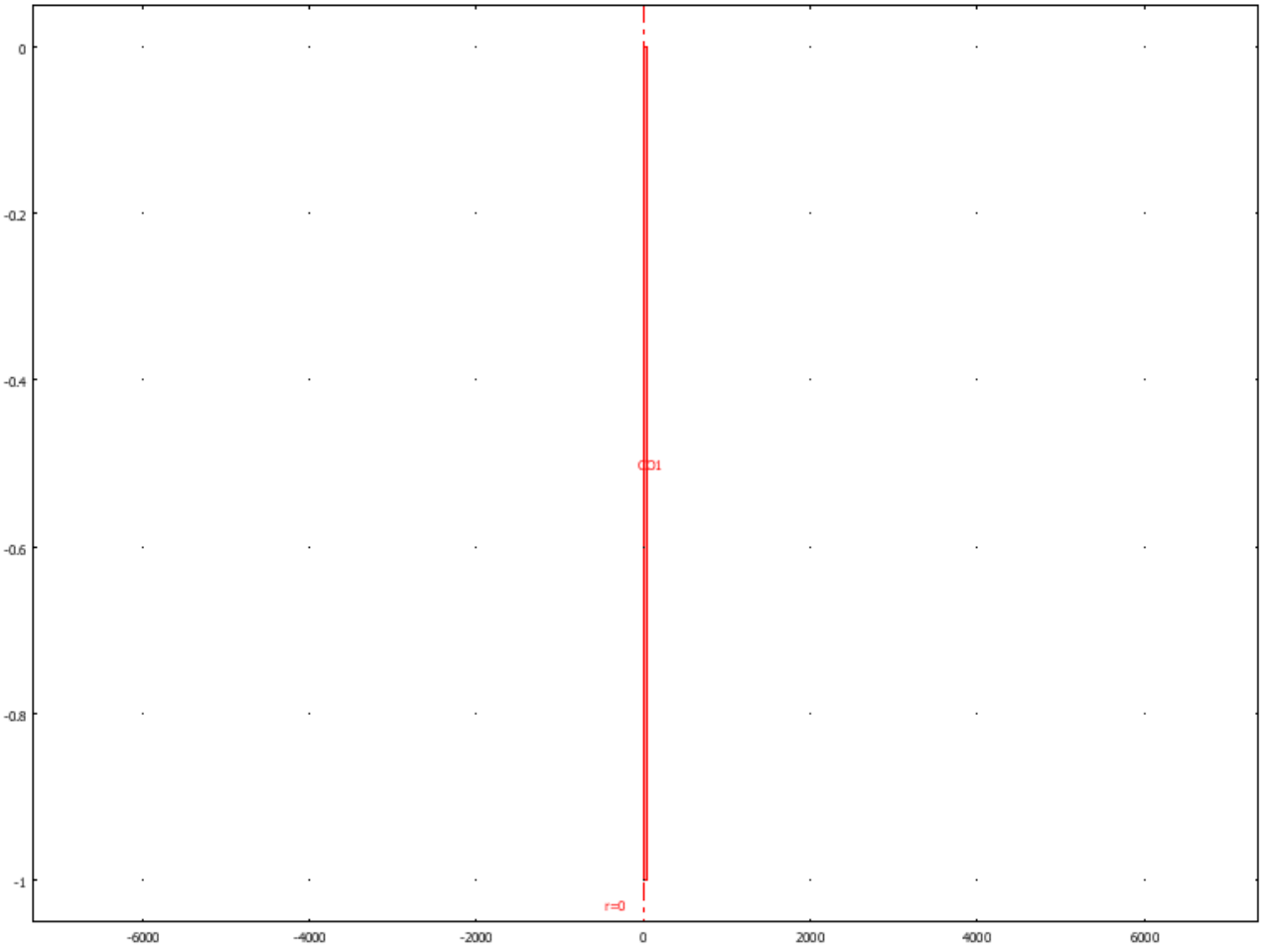


**Figure 16.** Geom. 1

### 3.1.1. Point mode

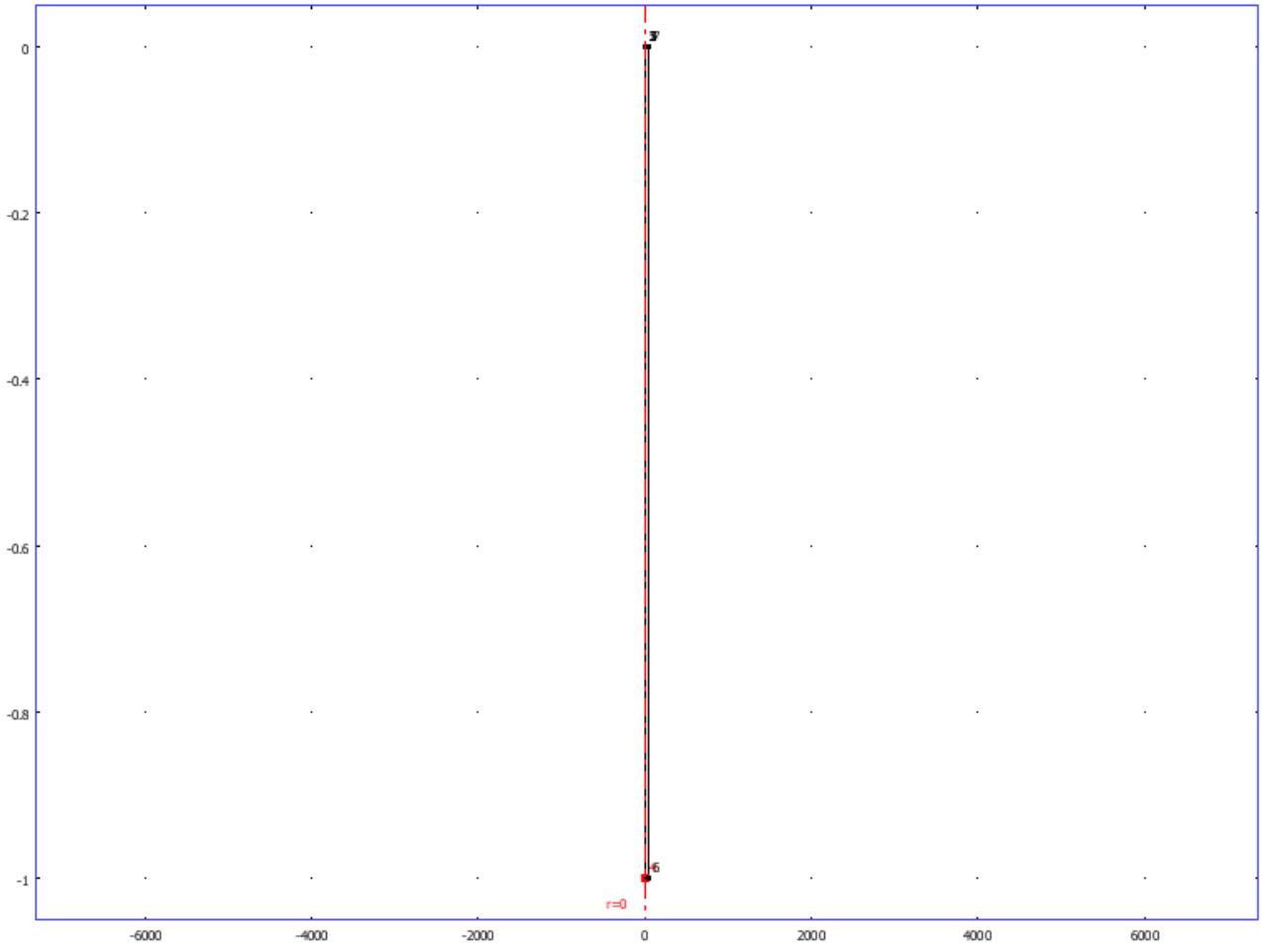


**Figure 17.** Point mode

### 3.1.2. Boundary mode

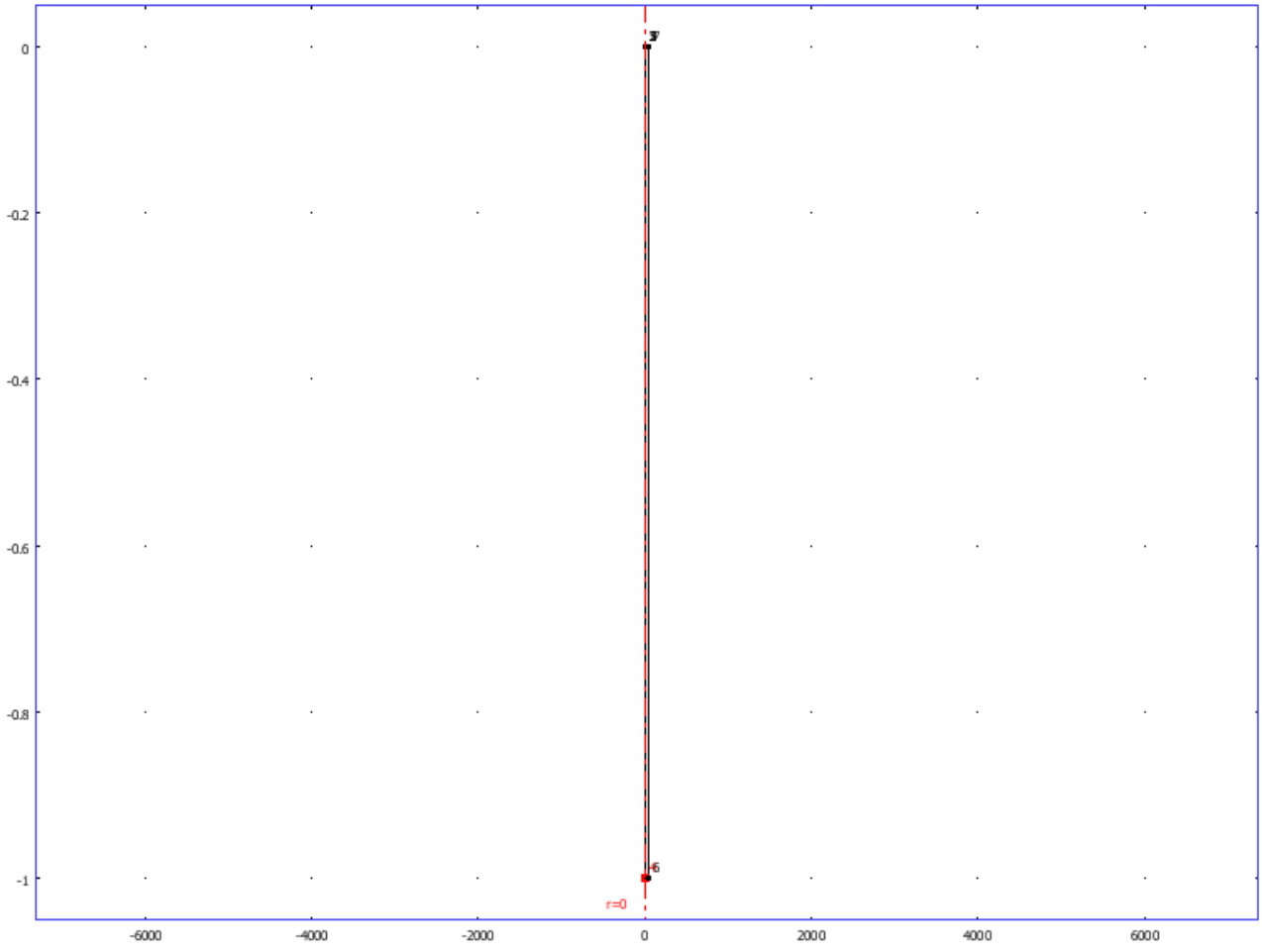


**Figure 18.** Boundary mode

### 3.1.3. Subdomain mode

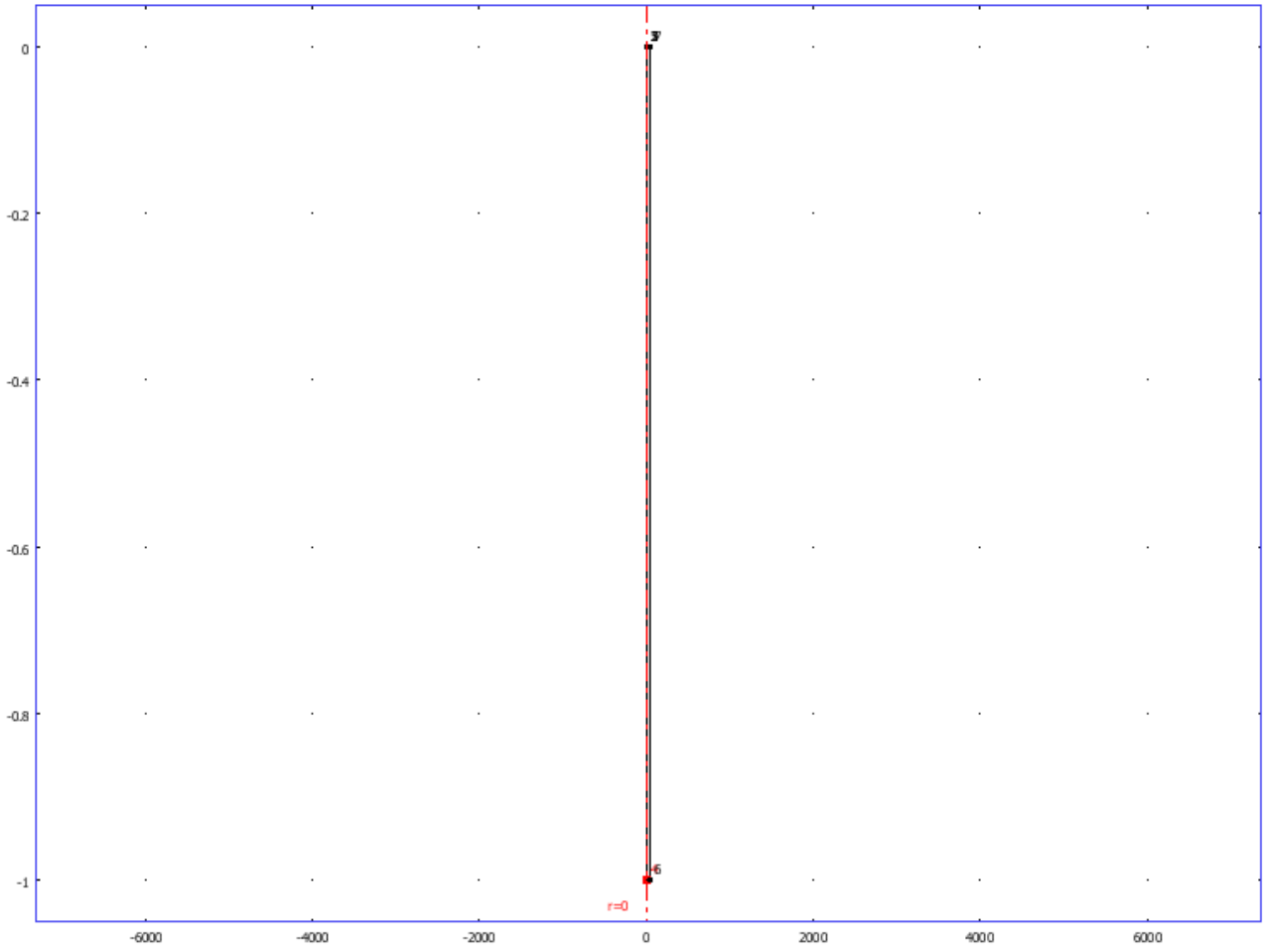


**Figure 19.** Subdomain mode

## 4.0 Geom 1

Space dimensions: Axial symmetry (2D)

Independent variables: r, phi, z

### 4.1 Scalar expressions

**Table 2.** Scalar expressions

| Name | Expression | Description |
|---|---|---|
| xi | 1 | |
| alpha | .5 | |
| K | 500 | |
| sigma | -0.000001 | |
| thetai | exp(0.5*38.92) | |
| thetal | exp(-0.5*38.92) | |
| S | (2/pi)*asin(sin(pi*sigma*t/2/log(thetal/thetai))) | |
| theta | (thetai^(1-S))*(thetal^S) | |
| tiptheta | exp(0.5*38.92) | |

## 4.2 Mesh

### 4.2.1 Mesh statistics

**Table 3** Mesh statics

| | |
|---|---|
| Number of degrees of freedom | 38090 |
| Number of mesh points | 5359 |
| Number of elements | 8328 |
| Triangular | 8328 |
| Quadrilateral | 0 |
| Number of boundary elements | 2388 |
| Number of vertex elements | 7 |
| Minimum element quality | 0.364 |
| Element area ratio | 0 |

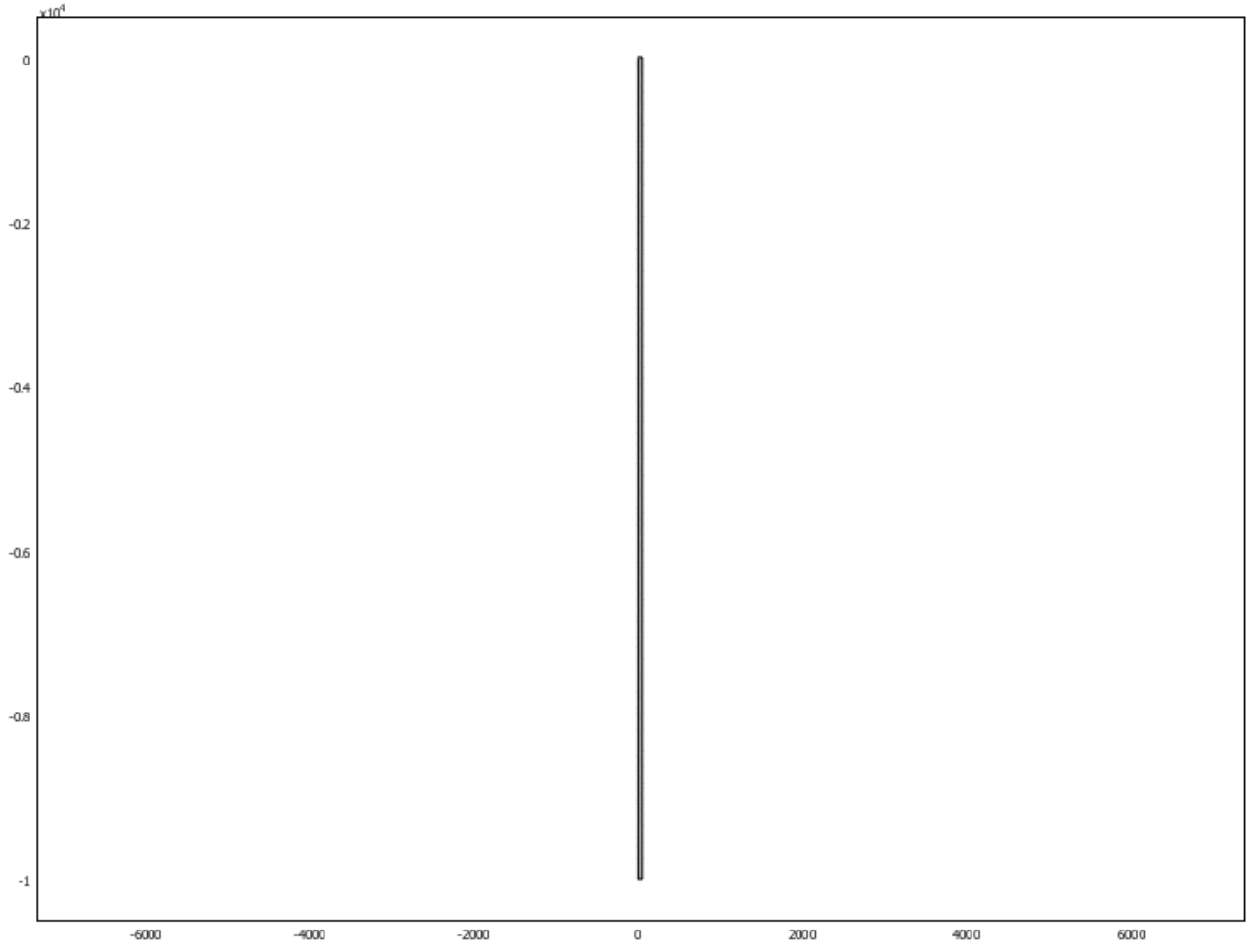


**Figure 20.** Mesh

### 4.3 Application mode: diffusion (di)

Application mode type: Diffusion (Chemical Engineering Module)

Application mode name: di

### 4.3.1. Application mode properties

**Table 4**. Application mode properties

| Property | Value |
|---|---|
| Default element type | Lagrange - Quadratic |
| Analysis type | Transient |
| Equilibrium assumption | Off |
| Frame | Frame (rz) |
| Weak constraints | Off |
| Constraint type | Ideal |

### 4.3.2. Variables

Dependent variables: c

Shape functions: shlag(2,'c')

Interior boundaries not active

### 4.3.3. Boundary settings

**Table 5.** Boundary settings

| Boundary | 1, 4-5, 7 | 2 | 3 |
|---|---|---|---|
| Type | Insulation/Symmetry | Flux | Flux |
| Mass transfer coefficient (kc) | 0 | **0.25*1000/(tiptheta^alpha)** | **0.25*K/(theta^alpha)** |
| Bulk concentration (cb) | 0 | **tiptheta*c2** | **theta*c2** |
| Concentration (c0) | 0 | 0 | 0 |

| Boundary | 6 |
|---|---|
| Type | Concentration |
| Mass transfer coefficient (kc) | 0 |
| Bulk concentration (cb) | 0 |
| Concentration (c0) | **1** |

### 4.3.4. Subdomain settings

**Table 6**. Subdomain settings

| | |
|---|---|
| Subdomain | 1 |
| Shape functions (shape) | **shlag(2,'c')** |
| Integration order (gporder) | **4** |
| Constraint order (cporder) | **2** |
| Diffusion coefficient (D) | **0.25** |

| | |
|---|---|
| Subdomain initial value | 1 |
| Concentration, c (c) | 1 |

### 4.4 Application mode: Diffusion (chdi)

Application mode type: Diffusion (Chemical Engineering Module)

Application mode name: chdi

### 4.4.1 Application mode properties

**Table 7.** Application mode properties

| Property | Value |
|---|---|
| Default element type | Lagrange - Quadratic |
| Analysis type | Transient |
| Equilibrium assumption | Off |
| Frame | Frame (rz) |
| Weak constraints | Off |
| Constraint type | Ideal |

### 4.4.2 Variables

Dependent variables: c2

Shape functions: shlag(2,'c2')

Interior boundaries not active

### 4.4.3 Boundary settings

**Table 8.** Boundary settings

| Boundary | 1, 4-5, 7 | 2 | 3 |
|---|---|---|---|
| Type | Insulation/Symmetry | Flux | Flux |
| Mass transfer coefficient (kc) | 0 | **0.25*1000*(tiptheta ^(1-alpha))** | **0.25*K*(theta ^(1-alpha))** |
| Bulk concentration (cb) | 0 | **c/tiptheta** | **c/theta** |
| Concentration (c0) | 0 | **(1-c)** | 0 |

| Boundary | 6 |
|---|---|
| Type | Concentration |
| Mass transfer coefficient (kc) | 0 |
| Bulk concentration (cb) | 0 |
| Concentration (c0) | 0 |

### 4.4.4 Subdomain Settings

Table 9. Subdomain settings

| | |
|---|---|
| Subdomain | 1 |
| Shape functions (shape) | **shlag(2,'c2')** |
| Integration order (gporder) | **4** |
| Constraint order (cporder) | **2** |
| Diffusion coefficient (D) | **0.25*xi*xi** |

## 5.0 Integration coupling variables

### 5.1 Geom.1

#### 5.1.1. Source boundary: 2

**Table 10.** Source boundary

| **Name** | **Value** |
|---|---|
| Variable name | I |
| Expression | 2*pi*r*ndflux_c_di |
| Order | 4 |
| Global | Yes |

### 5.1.2. Source boundary: 2

**Table 11.** Source boundary

| Name | Value |
|---|---|
| Variable name | I2 |
| Expression | 2*pi*r*ndflux_c2_chdi |
| Order | 4 |
| Global | Yes |

### 5.1.3. Source boundary: 3

**Table 12.** Source boundary

| Name | Value |
|---|---|
| Variable name | J |
| Expression | 2*pi*r*ndflux_c_di |
| Order | 4 |
| Global | Yes |

### 5.1.4. Source boundary: 3

**Table 13.** Source boundary

| Name | Value |
|---|---|
| Variable name | J2 |
| Expression | 2*pi*r*ndflux_c2_chdi |
| Order | 4 |
| Global | Yes |

## 6. 0 Solver setting

Solve using a script: off

**Table 14.** Solver settings

| | |
|---|---|
| Analysis type | Transient |
| Auto select solver | On |
| Solver | Time dependent |
| Solution form | General |
| Symmetric | Off |
| Adaptive mesh refinement | Off |
| Optimization/Sensitivity | Off |
| Plot while solving | Off |

## 6.1 Direct (UMFPACK)

Solver type: Linear system solver

**Table 15.** Linear system solver

| **Parameter** | **Value** |
|---|---|
| Pivot threshold | 0.1 |
| Memory allocation factor | 0.7 |

## 6.2 Time stepping

**Table 16.** Time stepping

| Parameter | Value |
|---|---|
| Times | range(0,97300*2,38920000*2) |
| Relative tolerance | 0.00001 |
| Absolute tolerance | 0.0000010 |
| Times to store in output | Specified times |
| Time steps taken by solver | Free |
| Maximum BDF order | 5 |
| Singular mass matrix | Maybe |
| Consistent initialization of DAE systems | Backward Euler |
| Error estimation strategy | Include algebraic |
| Allow complex numbers | Off |

## 6.3 Advanced

**Table 17.** Time stepping (advanced)

| Parameter | Value |
|---|---|
| Constraint handling method | Elimination |
| Null-space function | Automatic |
| Automatic assembly block size | On |
| Assembly block size | 5000 |
| Use Hermitian transpose of constraint matrix and in symmetry detection | On |
| Use complex functions with real input | Off |
| Stop if error due to undefined operation | On |
| Store solution on file | Off |
| Type of scaling | Automatic |
| Manual scaling | |
| Row equilibration | On |
| Manual control of reassembly | Off |
| Load constant | On |
| Constraint constant | On |
| Mass constant | On |
| Damping (mass) constant | On |
| Jacobian constant | On |
| Constraint Jacobian constant | On |

## 7.0 Postprocessing

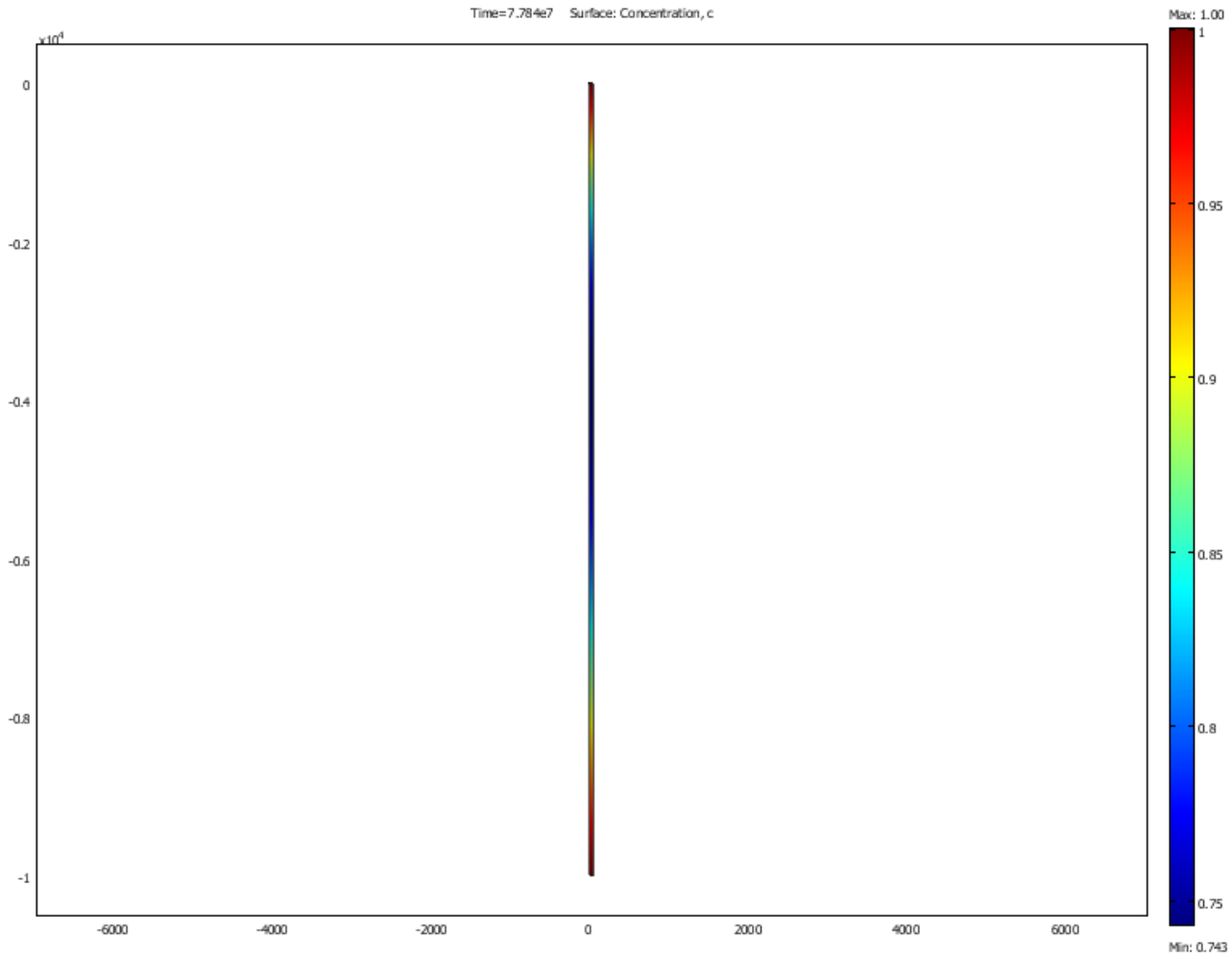


**Figure 21.** Postprocessing

## 8. 0 Variables

### 8.1 Boundary

**Table 18.** Boundary

| Name | Description | Expression |
|---|---|---|
| ndflux_c_di | Normal diffusive flux, c | nr_di * dflux_c_r_di+nz_di * dflux_c_z_di |
| ndflux_c2_chdi | Normal diffusive flux, c2 | nr_chdi * dflux_c2_r_chdi+nz_chdi * dflux_c2_z_chdi |

## 8.2 Subdomain

**Table 19.** Subdomain parametres

| Name | Description | Expression |
|---|---|---|
| grad_c_r_di | Concentration gradient, c, r component | cr |
| dflux_c_r_di | Diffusive flux, c, r component | -Drr_c_di * cr-Drz_c_di * cz |
| grad_c_z_di | Concentration gradient, c, z component | cz |
| dflux_c_z_di | Diffusive flux, c, z component | -Dzr_c_di * cr-Dzz_c_di * cz |
| grad_c_di | Concentration gradient, c | sqrt(grad_c_r_di^2+grad_c_z_di^2) |
| dflux_c_di | Diffusive flux, c | sqrt(dflux_c_r_di^2+dflux_c_z_di^2) |
| grad_c2_r_chdi | Concentration gradient, c2, r component | c2r |
| dflux_c2_r_chdi | Diffusive flux, c2, r component | -Drr_c2_chdi * c2r-Drz_c2_chdi * c2z |
| grad_c2_z_chdi | Concentration gradient, c2, z component | c2z |

| | | |
|---|---|---|
| dflux_c2_z_chdi | Diffusive flux, c2, z component | -Dzr_c2_chdi * c2r-Dzz_c2_chdi * c2z |
| grad_c2_chdi | Concentration gradient, c2 | sqrt(grad_c2_r_chdi^2+grad_c2_z_chdi^2) |
| dflux_c2_chdi | Diffusive flux, c2 | sqrt(dflux_c2_r_chdi^2+dflux_c2_z_chdi^2) |

## BIBLIOGRAPHY


(1) Bard, A. J., Mirkin, M. V; Scanning Electrochemical Microscopy; Eds.; Marcel Dekker: New York, 2001.

(2) P. Sun, F. Laforge, M.V. Mirkin, *Phys. Chem. Chem*. Phys. 2007, 9, 802

(3) R. M. Penner, M. J. Heben, T. L. Longin and N. S. Lewis, *Science*, 1990, 250, 1118.

(4) R. M. Penner, M. J. Heben and N. S. Lewis, *Anal. Chem.*, 1989, 61, 1630.

(5) M. V. Mirkin, F.-R. F. Fan and A. J. Bard, *J. Electroanal. Chem*., 1992, 328, 47.

(6) P. Sun and M. V. Mirkin, *Anal. Chem*. 2006, 78, 6526-6534

(7) J. Velmurugan, P. Sun, and M. V. Mirkin, *J. Phys. Chem*. C, 2009, 113, 459

(8) R. B. Morris, D. J. Franta and H. S. White, *J. Phys. Chem*., 1987, 91, 3559.

(9) J. D. Seibold, E. R. Scott and H. S. White, *J. Electroanal. Chem*., 1989, 264, 281.

(10) J. L. Conyers, Jr. and H. S. White, *Anal. Chem*., 2000, 72, 4441.

(11) J. J. Watkins and H. S. White, *Langmuir*, 2004, 20, 5474.

(12) S. Chen and A. Kucernak, *Electrochem. Commun*., 2002, 4, 80.

(13) S. Chen and A. Kucernak, *J. Phys. Chem*., 2002, 106, 9396.

(14) N. J. Gray and P. R. Unwin, *Analyst*, 2000, 125, 889

(15) B. Ballesteros Katemann, A. Schulte and W. Schuhmann, *Electroanalysis*, 2004, 16, 60.

(16) Laforge, F. o. O.; Velmurugan, J.; Wang, Y.; Mirkin, M. V. *Anal. Chem.* 2009, *81*, 3143

(17) Fan, F.-R. F.; Bard, A. J. *Proc. Natl. Acad. Soci. U.S.A.* 1999, *96*, 14222.

(18) F.F. Fan and A. J. Bard, *Science*, 1995, 267, 871
(19) F.-R. F. Fan, J. Kwak and A. J. Bard, *J. Am. Chem. Soc*., 1996, 118, 9669.

(20) Peng Sun and Michael V. Mirkin, *J. Am. Chem. Soc*. 2008, *130*, 8241

(21) Oldham, K. B. *Anal. Chem.* 1992, *64*, 646

(22) C. J. Slevin, N. J. Gray, J. V. Macpherson, M. A. Webb and P. R. Unwin, *Electrochem. Commun*., 1999, 1, 282.

(23) J. J. Watkins, J. Y. Chen, H. S. White, H. D. Abruna, E. Maisonhaute and C. Amatore, *Anal. Chem*., 2003, 75, 3962.

(24) J. J. Watkins and H. S. White, *Langmuir*, 2004, 20, 5474.

(25) Y. Shao, M. V. Mirkin, G. Fish, S. Kokotov, D. Palanker and A. Lewis, *Anal. Chem*., 1997, 69, 1627

(26) B. Ballesteros Katemann and W. Schuhmann, *Electroanalysis*, 2002, 14, 22.

(27) Bard, A. J.; Faulkner, L. R. Electrochemical Methods; Wiley: New York, 1980.

(28) Wightman, R. M.; Wipf, D. 0. In Electroanalytical Chemistry Bard, A. J., Ed.; Marcel Dekker: New York, 1989; Vol. 15, p 267.

(29) Bond, A. M.; Oldham, K. B.; Zoski, C. G. *Anal. Chim. Acta* 1989, 216, 177.

(30) Bard, A. J.; Mirkin, M. V.; Unwin, P. R.; Wipf, D. 0. *J. Phys. Chem*. 1992, 96, 1861.

(31) Oldham, K. B.; Myland, J. C.; Zoski, C. G.; Bond, A. M. J. *Electroanal. Chem. Interfacial Electrochem*. 1989, 270, 79.

(32) Rodgers, P. J.; Amemiya, S.; Wang, Y.; Mirkin, M. V. *Anal. Chem.* Submitted

(33) Wang, Y.; Mirkin, M. V.; Rodgers, P. J.; Kim, J.; Amemiya, S. *Anal. Chem.* Submitted

(34) Nan Yao, Focused Ion Beam: Basics and Applications, Cambridge; New York: Cambridge University Press, 2007

(35) Shoup, D.; Szabo, A. *J. Electroanal. Chem.* 1984, *160*, 27

(36) Zoski, C. G.; Mirkin, M. V. *Anal. Chem.* 2002, *74*, 1986

(37) Rodgers, P. J.; Amemiya, S. *Anal. Chem*. 2007, 79, 9276.

(38) McCreery, R. L. In Electroanalytical Chemistry; Bard, A. J., Ed.; Dekker, New York, 1991; Vol 17.
(39) Moore, A. In Chemistry and Physics of Carbon; Thrower, P. A., Ed., 1981; Vol 17.

(40) Richard L. McCreery, Chem. Rev. 2008, 108, 2646

(41) Iijima, *Nature*, 354, 56,1991

(42) I . Dumitresku, P.R.Unwin and J. V. Macpherson, *Chem. Communications*, 2009

(43) J. M. Nugent, K. S. V. Santhanam, A. Rubio and P. M. Ajayan, *Nano Lett.*, 2001, 1, 87

(44) Kim, J.; Hofmann, M.; Kong, J.; Amemiya, S. to be submitted.

(45) Heller, I.; Kong, J.; Williams, K. A.; Dekker, C.; Lemay, S. G. *J. Am. Chem. Soc*. 2006, 128, 7353

(46) Ronald J. Rice and Richard L. McCreery, *Anal. Chem*. 1989, 61, 1637

(47) Robert J. Bowling, Richard T. Packard, and Richard L. McCreery, *J. Am. Chem. Soc*. 1989, 111, 1217